

Classification of SARS-CoV-2 Variants through The Epistatistical Circos Plots with Convolutional Neural Networks

Bo Jing, Yu-Han Huang, and Hong-Li Zeng*

Nanjing University of Posts and Telecommunications, Nanjing, 210023, China and National Laboratory of Solid State Microstructures, Nanjing University, Nanjing, 210093, China

Erik Aurell†

*Department of Computational Science and Technology,
AlbaNova University Center, Stockholm, SE-106 91, Sweden*

The COVID-19 pandemic has profoundly affected global health, driven by the remarkable transmissibility and mutational adaptability of the SARS-CoV-2 virus. Five major variants of concern, Alpha, Beta, Gamma, Delta, and Omicron, have been identified. By August 2022, over 12.95 million full-length SARS-CoV-2 genome sequences had been deposited in the Global Initiative on Sharing Avian Influenza Data (GISAID) database, offering an unprecedented opportunity to investigate viral evolution and epistatic interactions. Recent advances in epistatic inference, exemplified by Direct Coupling Analysis (DCA) (Zeng et al., Phys. Rev. E, 2022), have generated numerous Circos plots illustrating genetic inter-dependencies. In this study, we constructed a dataset of 1,984 Circos plots and developed a convolutional neural network (CNN) framework to classify and identify the corresponding genomic variants. The CNN effectively captured complex epistatic features, achieving an accuracy of 99.26%. These findings demonstrate that CNN-based models can serve as powerful tools for exploring higher-order genetic dependencies, providing deeper insights into the evolutionary dynamics and adaptive mechanisms of SARS-CoV-2.

keywords: SARS-CoV-2 | Convolution neural network | Direct coupling analysis (DCA) | Epistasis | Circos plots

I. INTRODUCTION

The COVID-19 pandemic, caused by the severe acute respiratory syndrome coronavirus 2 (SARS-CoV-2), has posed an unprecedented global health crisis since its emergence in late 2019. The virus exhibits remarkable transmissibility and mutational adaptability, which have enabled it to spread rapidly and persist across diverse populations. Over the pandemic period, several major variants of concern (VOCs) including Alpha, Beta, Gamma, Delta, and Omicron have been identified by the World Health Organization, each characterized by distinct combinations of mutations associated with enhanced infectivity, immune escape, or altered pathogenicity [1, 2]. Understanding the evolutionary mechanisms underlying these adaptive features is critical for developing effective surveillance strategies, guiding vaccine updates, and anticipating future viral dynamics.

The advent of high-throughput sequencing technologies has generated a large amount of viral genomic data. Until August 2022, the GISAID repository contained more than 12.95 million high-quality SARS-CoV-2 genome sequences [3]. This vast dataset offers an exceptional opportunity to study the evolutionary trajectories of SARS-CoV-2 at the molecular level. Beyond identifying single mutations or lineage-defining substitutions, researchers have increasingly focused on the epistatic interactions—non-additive effects arising from

interdependent mutations—that shape the virus’s adaptive landscape. Such epistasis can modulate viral fitness, alter host-pathogen interactions, and influence antigenic drift, thereby serving as a key driver of viral evolution [4, 5].

To uncover these epistatic relationships, various computational frameworks have been developed, among which Direct Coupling Analysis (DCA) has gained particular prominence. Originating from statistical physics, DCA infers residue–residue coevolution by estimating direct information couplings between positions in multiple sequence alignments [6–8]. Recent applications of DCA to SARS-CoV-2 have revealed complex epistasis of mutations through the genomic sequences [9–11]. The results are often visualized as Circos plots [12], which display pairwise genetic couplings across the viral genome. These circular representations allow researchers to intuitively inspect patterns of co-variation and potential functional dependencies. However, as the scale of genomic data and the number of variants continue to grow, manual inspection and traditional statistical evaluations of these Circos plots become increasingly inefficient.

To address this challenge, there is a growing need for automated, scalable, and data-driven approaches capable of detecting and classifying complex epistatic patterns embedded in visual data. Notably, Circos plots that represent genome-wide epistatic interactions can be regarded as structured images in which spatial arrangements and link densities encode biologically meaningful relationships. Therefore, identifying variant-specific epistatic signatures becomes essentially a pattern recognition problem in a high-dimensional visual space.

* hlzeng@njupt.edu.cn

† eaurell@kth.se

Recent advances in deep learning, particularly convolutional neural networks (CNNs), have demonstrated extraordinary success in image recognition, natural pattern extraction, and multidimensional data analysis. CNNs are designed to hierarchically learn spatial features from raw visual inputs, allowing them to capture both local and global dependencies without the need for hand-crafted feature engineering [13, 14]. In bioinformatics, deep convolutional and representation-learning architectures have been successfully applied to problems such as protein structure prediction, chromatin interaction mapping, and molecular phenotype classification [15–17].

Inspired by the above insights, we propose to leverage CNNs to analyze Circos plots derived from DCA method over the genomic sequences of SARS-CoV-2 [10], thereby enabling the automated identification of genomic variants through their epistatic signatures. By treating Circos plots as structured visual representations of co-mutation networks, CNNs can learn the features of the spatial configurations corresponding to different evolutionary lineages. Here we constructed a dataset of 1,984 Circos plots encompassing five major VOCs and developed a tailored CNN classification framework to classify the variants. The trained model achieved a classification accuracy of 99.26%, demonstrating its ability to extract and generalize the complex interaction features encoded in the Circos visualizations.

Our results indicate that CNNs can serve as powerful tools for detecting higher-order genetic dependencies, offering a novel avenue for quantitative epistasis inference from large-scale genomic data. Furthermore, this approach bridges the gap between statistical physics-based evolutionary modeling and artificial intelligence, providing a scalable and interpretable framework for exploring viral coevolution. By integrating DCA-based inference with deep learning-based visual recognition, we aim to advance our understanding of how interdependent mutations shape the adaptive mechanisms of SARS-CoV-2 and potentially other rapidly evolving RNA viruses.

The remainder of this paper is organized as follows. Section 2 describes the framework of Direct Coupling Analysis (DCA) and the construction of our dataset. Section 3 presents the CNN architectures adopted in our study—VGG, MobileNet, DenseNet, and EfficientNet, while Section 4 provides the experimental results and evaluation criteria. Finally, Section 5 concludes the study and outlines perspectives for future development.

II. MATERIALS AND METHODS

A. Data Collection

All genome sequences analyzed here were retrieved from GISAID [3, 18], which has evolved into one of the most important repositories for SARS-CoV-2 genomics. It has continuously aggregated vast amounts of high-quality genome sequences submitted by research institu-

tions and public health laboratories worldwide, thereby providing an indispensable foundation for large-scale studies on viral evolution, mutation tracking, and epidemiological surveillance. To date, millions of complete SARS-CoV-2 genome sequences have been deposited in GISAID, providing an unparalleled resource for tracking viral evolution. However, due to a temporal delay between sample collection and sequence submission [19], the database reflects viral dynamics with a slight time lag. To ensure robust temporal representation, we therefore compiled as comprehensive a dataset as possible, covering diverse sampling periods and geographic regions.

To keep the analysis consistent with [10], we employ the same dataset covering the period from late 2019 to August 23, 2022, as the number of new genome submissions to GISAID declined significantly thereafter. We collected 5,465,988 high-quality, full length genome sequences (approximately 30 kbp each) from GISAID for analysis. To ensure temporal consistency, the sequences were stratified on a daily basis, yielding data spanning 962 consecutive days. The number of entries per day reflects the volume of genome submissions to GISAID as of the above date.

Each entry in the GISAID database is accompanied by detailed metadata, including gender, age, geographic region, and viral lineage, which provide valuable contextual information for the following classification and comparative analyses.

B. Data Preprocessing

1. Data Collection

This section details the data preprocessing framework used in this study. Specifically, raw SARS-CoV-2 genomic sequences retrieved from GISAID were subjected to systematic cleaning, alignment, and quality filtering to construct high-confidence multiple sequence alignments (MSAs). Subsequently, the Direct Coupling Analysis (DCA) method was applied to infer epistatic interactions between genomic loci, which were then visualized using the Circos software [12]. The structured visual epistasis is required for downstream deep-learning-based classification and variant identification.

Figure 1 illustrates the temporal distribution of SARS-CoV-2 genome sequences across different variants between December 2019 and August 2022. The number of sequences exhibits clear temporal clustering corresponding to the global emergence of distinct variants. The Alpha wave peaked in early 2021 and was subsequently replaced by Delta in mid-2021, while Omicron became dominant after November 2021, producing the highest sequencing counts. In contrast, Beta and Gamma remained relatively limited throughout the period. The Else category represents other minor or unclassified lineages that persisted at low levels. The gradual decrease in sequence submissions after mid-2022 indicates a decline in global

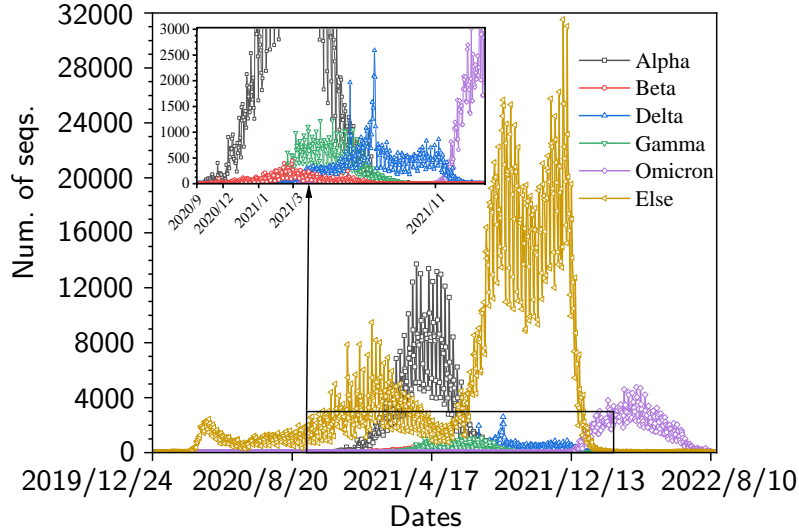


FIG. 1: Temporal distribution of SARS-CoV-2 genome sequences by variants. The main panel shows the daily number of sequences collected from the GISAID database between December 2019 and August 2022, classified into the major variants of concern (Alpha, Beta, Gamma, Delta, and Omicron) and other minor lineages (Else). Distinct temporal waves correspond to the global emergence and dominance of each variant: Alpha surged in early 2021, Delta dominated mid-2021, and Omicron replaced all previous variants after late 2021. The inset highlights the early coexistence of Alpha, Beta, and Gamma variants. The sequencing volume declines after mid-2022, reflecting reduced global sequencing activity and fewer new submissions to GISAID.

genomic surveillance and GISAID data reporting. The temporal distribution of variations highlights the differing evolutionary dynamics and data availability among the major variants.

The genomic data were classified according to variant type and sampling date using a MATLAB-based preprocessing pipeline, which generated sub-datasets for each strain and time interval. Since DCA requires a sufficient sample size to reliably infer epistatic interactions, all sub-datasets containing 150 or fewer sequences were excluded. With such filtering, a total of 906,292 Alpha sequences (259 days), 119,855 Delta sequences (259 days), 414,728 Omicron sequences (224 days), and 4,016,078 Else sequences (700 days) were retained for downstream analysis.

2. Sequence Alignment and loci filtering

All remained raw genomic sequences within each variant group were aligned using multiple sequence alignment (MSA) to ensure positional correspondence across nucleotide sites. Here the online server MAFFT [20, 21] was used to perform the alignment with “Wuhan-Hu-1” [22] serving as the reference sequence. Such manipulation not only speeds up the alignment but also reduces the burden on computational resources.

With the obtained MSAs, each sub dataset can be represented as a large matrix $S = \{\sigma_i^n | i = 1, 2, \dots, N\}$, where N denotes the number of aligned genomic se-

quences in the sub dataset and L the number of loci. Here $L = 29,903$ which has the same length with the reference sequence. Each loci σ_i^n of the matrix S can take six possible states: four main nucleotides (A, G, C, T), an “unknown nucleotide” (N), or an alignment gap (-) introduced to handle nucleotide deletions or insertions [23]. For computational convenience, these states (“-NAGCT”) were numerically encoded as (0–5) to facilitate inferring processing.

To remove non-informative positions and reduce redundancy in the epistatic inference, we applied a two-stage filtering strategy controlled by a threshold parameter ϕ (expressed as a percentage). First, for each column in the MSA, if the frequency of the most dominant nucleotide exceeded ϕ , the corresponding locus was considered overly conserved and removed. Second, for each sequence, if the frequency of any single nucleotide exceeded ϕ , or if the total fraction of canonical bases (A, C, G, and T) was less than or equal to $1-\phi$, that sequence was excluded.

This filtering process effectively eliminated loci with low mutational variability and sequences with poor information content, thereby improving the robustness and computational efficiency of subsequent DCA-based epistasis analysis. The variation in the number of retained loci under different thresholds for each viral variant is illustrated in Fig. 2. The choice of the filtering threshold ϕ plays a critical role in balancing data completeness and sequence variability. A higher threshold removes highly conserved loci, thereby focusing the analysis on positions

with greater mutational potential, whereas an excessively high threshold may discard too many loci and reduce the effective sequence coverage. Conversely, a lower threshold retains more data but increases redundancy and noise from invariant sites, which can obscure the detection of genuine epistatic couplings.

To evaluate the impact of ϕ , we systematically tested several threshold values ranging from 0.90 to 0.99 and analyzed the number of surviving loci for each SARS-CoV-2 variant (Fig. 2). The number of retained loci increases monotonically with ϕ , indicating that a higher threshold selectively removes conserved genomic positions and retains those exhibiting greater sequence diversity. Among the four analyzed variants, Omicron exhibits the largest number of surviving loci across all thresholds, suggesting a higher degree of nucleotide variability, while Alpha remains the most conserved. The curves also show a pronounced rise beyond $\phi = 0.96$, reflecting the nonlinear effect of the threshold on dataset size and emphasizing the importance of selecting an optimal ϕ for balancing data quality and sample quantity. To ensure sufficient sample size while maintaining data quality, we combined the datasets obtained under the thresholds $\phi = 0.95$ and 0.96, providing an optimal compromise between data completeness and sequence diversity.

3. Direct Coupling Analysis

The Direct Coupling Analysis (DCA), otherwise alternatively referred to as maxentropy methods, inverse statistical mechanics or model inference in an exponential family, means to learn a probabilistic model of the Gibbs-Boltzmann type from data, and then to use the parameters of this model to predict a quantity of interest. When the model is limited to linear and quadratic terms the probability distribution is equivalent to the equilibrium distribution of an Ising or Potts model, and can be written

$$P(\sigma) = \frac{1}{Z} \exp \left\{ \sum_i h_i(\sigma_i) + \sum_{ij} J_{ij}(\sigma_i, \sigma_j) \right\}, \quad (1)$$

In above σ denotes a L -dimensional vector of data, the parameters $h_i(\sigma_i)$ encode effects which only depend on the data (σ_i) at one position i , and $J_{ij}(\sigma_i, \sigma_j)$ encode effects which depend on the data (σ_i, σ_j) at two positions i and j . The total data then consists of N data vectors, typically assumed to be independent draws of the same probability distribution, such that the total probability is the product of N functions as in (1), where the argument of the r 'th term in the product is the r 'th draw $\sigma^{(r)}$:

$$P \left(\{\sigma^{(r)}\}_{r=1}^N \right) = \prod_{r=1}^N P \left(\sigma^{(r)} \right) = \frac{1}{Z^N} \exp \left\{ N \sum_{i,s} \langle h_i(s) \rangle + N \sum_{ij,ss'} \langle J_{ij}(s, s') \rangle \right\} \quad (2)$$

where $\langle h_i(s) \rangle$ stands for $\frac{1}{N} \sum_{r=1}^N h_i(s) \mathbf{1}_{\sigma_i^{(r)}, s}$ and $\langle J_{ij}(s, s') \rangle$ stands for $\frac{1}{N} \sum_{r=1}^N J_{ij}(s, s') \mathbf{1}_{\sigma_i^{(r)}, s} \mathbf{1}_{\sigma_j^{(r)}, s'}$. The original and still most important instance of DCA is learning a model of a protein family, where each $\sigma^{(r)}$ stands for the amino acid sequence of protein r , and the arity of each argument is 20 (number of amino acids), or more often 21 (including a gap variable in a multiple sequence alignment) [24, 25], for extensions to protein complexes see [8, 26]. Large values of J_{ij} (evaluated in a suitable norm) are then good predictors of spatial proximity in the protein structure or between proteins. DCA has been reviewed multiple times from the algorithmic point of view, see e.g. [27, 28].

The underlying principle of why DCA works, *e.g.* why the terms in the probabilistic model is a better predictor than straightforward correlations has been much debated *cf.* [29, 30]. Given the diverse nature of biological sequences to which DCA has been applied, pertaining to phenomena developing on very different time scales, there may be different underlying mechanisms in different cases. In particular, DCA may not always be a reasonable inference procedure if actually the underlying distribution is not close to (1).

In population genetics, the quasi-linkage equilibrium (QLE) framework provides a statistical description of weakly interacting loci under conditions of moderate recombination and weak selection. In this regime, linkage disequilibrium (LD) between loci can be approximated by a linear response to the underlying epistatic interaction coefficients, allowing the genotype distribution to be expressed as a perturbation around an uncorrelated (product) distribution [31–35]. Mathematically, the distribution of individuals over genotypes in a population are then of the Gibbs-Boltzmann form, *i.e.* as in (1). However, in contrast to other approaches where the parameters h_i and J_{ij} are directly interpreted as fitness effects, in the setting of QLE they are derived compound parameters expressible in terms of fitness effects and mutation and recombination rates [36]. For instance, the relation between J_{ij} and epistatic fitness parameters f_{ij} depends parametrically on mutation rates, and is different at high and low mutation rates [35]. Furthermore, at sufficiently low recombination rates the distribution of individuals over genotypes is not of the exponential type but closer to a mixture model, a phenomenon referred to as clone competition [32, 33, 37]. Although QLE hence simplifies the biological reality by assuming weak selection and moderate recombination, it provides a practical statistical foundation for extracting meaning-

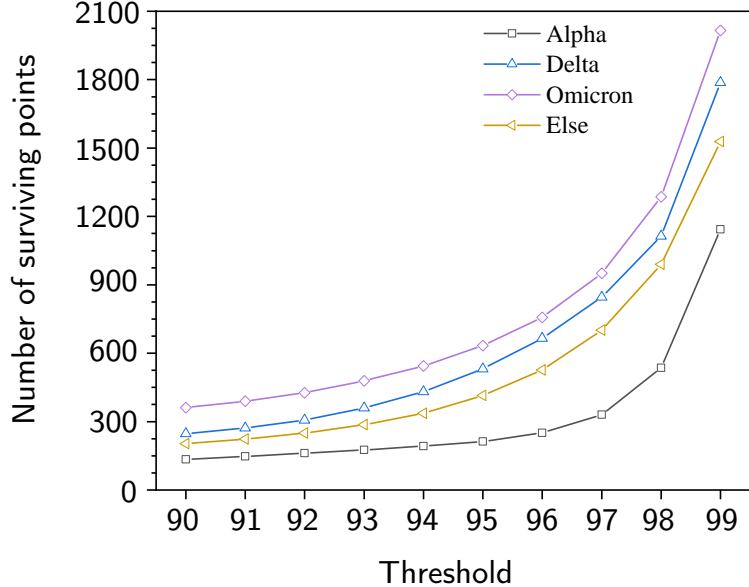


FIG. 2: Effect of filtering threshold on the number of surviving loci for four variant categories. With the threshold ϕ increases from 0.90 to 0.99, the number of surviving loci rises steadily, reflecting the progressive removal of highly conserved sites. Among all variants, Omicron consistently retains the largest number of loci, followed by Delta, Else, and Alpha, indicating higher overall sequence variability in Omicron and Delta compared to Alpha. A near-exponential growth in surviving loci is observed when $\phi > 0.96$, demonstrating the sensitivity of the dataset size to the chosen conservation threshold.

ful co-evolutionary information from large-scale genomic datasets.

Here we employed the pseudo-likelihood maximization (PLM) approach, a computationally efficient variant of DCA, to infer probabilistic relations between loci from aligned MSA [34, 38–42]. The PLM method estimates the coupling parameters by maximizing the conditional probability of each site given all other sites in the alignment. For a Potts model with multiple states ($q > 2$), the conditional probability of site i takes the form:

$$P(\sigma_i|\sigma_i) = \frac{\exp\left(h_i(\sigma_i) + \sum_{j \neq i} J_{ij}(\sigma_i, \sigma_j)\right)}{\sum_u \exp\left(h_i(u) + \sum_{j \neq i} J_{ij}(u, \sigma_j)\right)}, \quad (3)$$

with $u = \{0, 1, 2, 3, 4, 5\}$ as the possible states of σ_i . For data consisting of N sequences PLM amounts to separately maximizing L functions

$$\begin{aligned} PL_i(h_i, \{J_{ij}\}) = & \frac{1}{N} \sum_s h_i(\sigma_i^{(s)}) \\ & + \frac{1}{N} \sum_s \sum_{j \neq i} J_{ij}(\sigma_i^{(s)}, \sigma_j^{(s)}) \\ & - \frac{1}{N} \sum_s \log \sum_u \exp \left(h_i(u) + \sum_{j \neq i} J_{ij}(u, \sigma_j^{(s)}) \right) \end{aligned} \quad (4)$$

with s labeling the sequences from 1 to N . An adjustment procedure is applied afterwards to reconcile the two in principle different values obtained for J_{ij} from maximizing respectively $P(\sigma_i|\sigma_i)$ or $P(\sigma_j|\sigma_j)$. Additionally, regularization, typically an L_2 penalty, is used. By optimizing these sums of log-conditional probabilities in eq. (4) over all sites and sequences, PLM efficiently estimates the local fields and coupling parameters, allowing for accurate inference in high-dimensional genomic datasets where exact likelihood maximization by eq. (2) is computationally infeasible.

We here take the inferred parameters J_{ij} as proxies for epistatic fitness parameters. In the setting of QLE this corresponds to the low mutation rate inference formula $f_{ij}^* = rc_{ij}J_{ij}^*$ [31–33] and ignoring the overall numerical factor r (recombination rate) and loci-specific factor c_{ij} (related to genomic distance between i and j). With PLM the interaction between loci i and j was scored by Frobenius parametric number. To extract the most informative epistatic interactions from the SARS-CoV-2 genome, we selected the top 200 locus pairs with the highest coupling scores inferred by DCA. The genomic positions of the corresponding nucleotides were mapped by aligning them to the reference sequence “Wuhan-Hu-1”. These pairwise interactions were subsequently visualized using the Circos software [12], resulting in a comprehensive graphical representation of the epistatic network across the SARS-CoV-2 genome, as illustrated in Fig. 3.

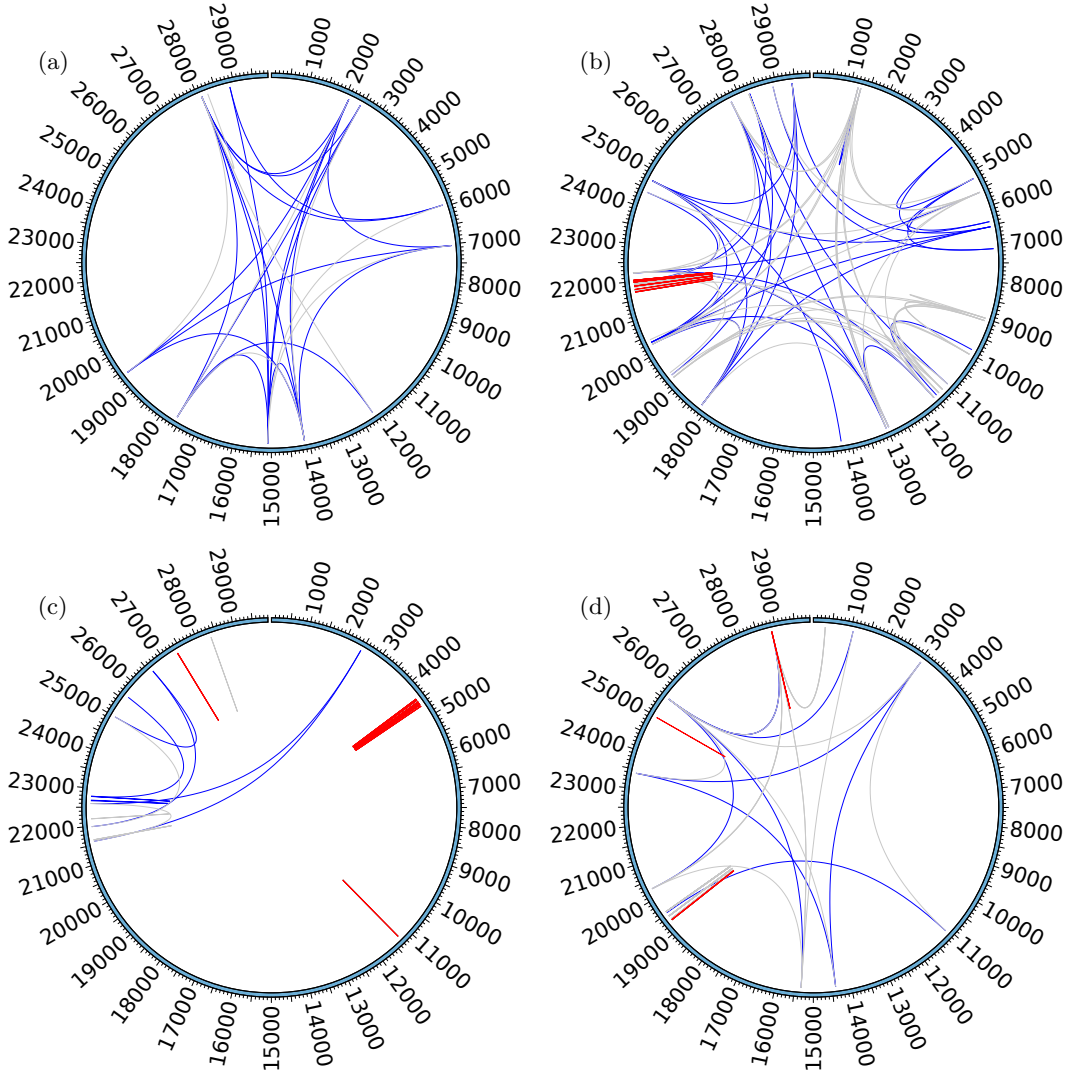


FIG. 3: The graph is an image of the epistasis of data sets, with the line segments indicating the top 200 significant pairwise epistasis between the coding region motifs in the data set for this date. The colored lines indicate the top 50, and the gray lines indicate the top 51 to 200. Red lines indicate short-distance connections (distance less than or equal to 3 bp); blue lines indicate longer distances. Threshold $\phi=95\%$, (a) Alpha; (b) Delta; (c) Omicron; (d) Else.

Based on the filtering thresholds of $\phi = 0.95$ and $\phi = 0.96$, the number of generated epistatic interaction (Circos) images varied across different variants. To ensure balanced representation, we randomly selected approximately 500 images from each variant category, resulting in a total of 1,984 images used for training the convolutional neural network (CNN). The dataset was randomly divided into 80% for training and 20% for validation to optimize model performance. A detailed distribution of the images across different variants is provided in Table I. The dataset is representative of the overall image population generated by our analysis pipeline, and similar Circos plots used for CNN training are publicly available in the GitHub repository [43].

TABLE I: Data set description

Class	Train	Test	Total
Alpha	415	103	518
Delta	415	103	518
Omicron	359	89	448
Else	400	100	500

C. Methods for image classification

To classify the Circos plots representing SARS-CoV-2 epistatic interactions, we employed four representative convolutional neural network (CNN) architectures [44]: VGG13 and 16, MobileNetV2, DenseNet121, and Ef-

ficientNetB0. These networks embody distinct design philosophies across different generations of CNN research, allowing for a comprehensive comparison of depth, connectivity, and computational efficiency.

1. VGG

The VGGNet family, introduced by Simonyan and Zisserman in 2014 [45], represents one of the most classical and widely adopted convolutional neural network (CNN) architectures for visual feature extraction. It is built on the principle of stacking small 3×3 convolutional kernels with stride 1 and padding 1, followed by 2×2 max-pooling layers with stride 2. This design enables a deep yet computationally efficient network that progressively captures spatial hierarchies from low to high level features.

Among the VGG variants, VGG13 and VGG16 mainly differ in network depth: VGG13 contains 13 weight layers (11 convolutional and 2 fully connected), whereas VGG16 extends to 16 weight layers (13 convolutional and 3 fully connected). Both models are composed of five convolutional blocks, where the number of filters doubles after each block (64, 128, 256, 512, and 512). The extracted feature maps are flattened and passed through two fully connected layers with 4096 neurons each, followed by a Softmax layer for multi-class classification. Generally, VGG provides a baseline for feature extraction and image classification, serving as a reference point for deeper and more efficient designs.

2. MobileNet

MobileNets [46], is a lightweight CNN architecture specifically designed for efficient computation on limited-resource environments while maintaining high accuracy. Unlike traditional CNNs that rely on standard convolution operations, MobileNet adopts depthwise separable convolutions to decouple spatial and channel-wise filtering. This operation drastically reduces the number of trainable parameters and computational cost, achieving a balance between accuracy and efficiency.

Here the third generation of the MobileNet family, MobileNetV3 [47], was fine-tuned on the SARS-CoV-2 Circos image dataset using ImageNet pre-trained weights. MobileNetV3 integrates neural architecture search (NAS), Squeeze-and-Excitation (SE) attention modules, and the hard-swish activation function to further enhance feature expressiveness and computational efficiency. These refinements enable the model to achieve high accuracy with minimal parameters, making it particularly effective for large-scale image classification under constrained resources.

3. DenseNet

DenseNet, proposed by Huang et al. in 2017 [48], is a deep CNN that introduces the concept of dense connectivity to enhance feature reuse and gradient propagation across layers. Unlike traditional feed-forward architectures, where each layer receives input only from its immediate predecessor, DenseNet establishes direct connections from each layer to all subsequent layers. Formally, the feature map of the l -th layer is defined as

$$x_l = H_l([x_0, x_1, \dots, x_{l-1}]),$$

where $[x_0, x_1, \dots, x_{l-1}]$ denotes the concatenation of feature maps produced by all previous layers, and $H_l(\cdot)$ represents a composite function consisting of Batch Normalization, ReLU activation, and 3×3 convolution.

The dense connectivity pattern alleviates the vanishing-gradient problem, promotes efficient feature reuse, and significantly reduces the number of parameters compared with networks of similar depth. DenseNet121 is composed of four dense blocks connected by transition layers, which perform 1×1 convolutions followed by 2×2 average pooling to control feature-map dimensions and computational cost. DenseNet121 facilitates efficient feature reuse and robust gradient propagation, leading to improved representational capacity with fewer parameters.

4. EfficientNet

EfficientNetB0, proposed by Tan and Le in 2019 [49], represents a new generation of CNN optimized through compound scaling. Unlike traditional approaches that scale depth, width, or input resolution independently, EfficientNet employs a unified scaling strategy that jointly adjusts all three dimensions using a small set of fixed coefficients. This design allows the network to achieve an optimal trade-off between accuracy and computational efficiency, outperforming previous architectures with significantly fewer parameters and floating-point operations.

EfficientNetB0 is the baseline model of the EfficientNet family, discovered via neural architecture search (NAS) and subsequently scaled to larger versions (B1–B7). Its backbone structure consists of a series of mobile inverted bottleneck convolution (MBConv) blocks, which incorporate depthwise separable convolutions, squeeze-and-excitation (SE) attention modules, and the swish activation function. The MBConv design effectively reduces computational redundancy while maintaining high representational capacity, and the SE blocks dynamically recalibrate feature responses to emphasize informative channels.

The above models was fine-tuned under identical training settings as detailed in the following Section, ensuring consistent optimization and fair comparison across all employed models.

TABLE II: Hyperparameter settings for different networks models

Model	Epoch	Activation function	Batch Size	Loss function	Optimizer	Learning rate
VGG-13	100	Softmax	16	CrossEntropy	SGD	0.003125
VGG-16	100	Softmax	16	CrossEntropy	SGD	0.003125
MobileNetV3	100	Softmax	16	CrossEntropy	SGD	0.003125
DenseNet121	100	Softmax	16	CrossEntropy	SGD	0.003125
EfficientNet_B0	100	Softmax	16	CrossEntropy	SGD	0.00625

5. Model Training Configuration

The setting of hyperparameters plays a crucial role in determining the performance of deep learning models. Therefore, a series of experiments were conducted to select the most suitable hyperparameter configuration for all CNN architectures. Specifically, the learning rate, batch size, and number of iterations were systematically adjusted to identify the optimal setup. The final hyperparameter settings are summarized in Table II.

All models were implemented using the TensorFlow 2.12 framework with GPU acceleration and were initialized with ImageNet pre-trained weights. The input Circos images were uniformly resized to $224 \times 224 \times 3$, normalized to the $[0, 1]$ range, and augmented with random rotation, horizontal flipping, and brightness adjustment to improve generalization. The stochastic gradient descent (SGD) optimizer with a momentum of 0.9 was employed, and the initial learning rate was set to 0.003125 while 0.00625 for the EfficientNet_B0. The learning rate was decayed by a factor of 0.1 every 30 epochs (i.e., at epochs 30, 60, and 90).

The models were trained using a batch size of 16 for up to 100 epochs, and the categorical cross entropy loss function was used for multi-class classification. To prevent overfitting and optimize computational resource utilization, early stopping was applied when the validation loss failed to improve for 10 consecutive epochs. In addition, the training process was automatically suspended when the loss value stabilized, preventing unnecessary cost over computational resources. Each experiment was 3 three times with different random seeds, and the reported results represent the mean performance across runs to ensure reproducibility and robustness.

III. MODEL EVALUATION AND PERFORMANCE ANALYSIS

To comprehensively assess model performance and generalization capability, five CNN architectures, VGG16, MobileNetV2, MobileNetV3, DenseNet121, and EfficientNet_B0, were trained and validated on the SARS-CoV-2 Circos image dataset. All models were optimized under identical hyperparameter configurations described in Table II to ensure a fair and consistent comparison across architectures.

Model performance was quantitatively evaluated using standard classification metrics, including accuracy, precision, recall, F_1 -score, and the area under the receiver operating characteristic curve (AUC-ROC), as defined in the following formulae.

$$\text{Accuracy} = \frac{TP + TN}{TP + FP + TN + FN}, \quad (5)$$

$$\text{Recall} = \frac{TP}{TP + FN}, \quad (6)$$

$$\text{Precision} = \frac{TP}{TP + FP}, \quad (7)$$

$$F_1\text{-score} = 2 \times \frac{\text{Precision} \times \text{Recall}}{\text{Precision} + \text{Recall}} \quad (8)$$

where TP , TN , FP , and FN denote the numbers of true positives, true negatives, false positives, and false negatives, respectively. Accuracy measures the overall proportion of correctly classified samples and reflects the model's general predictive capability. Recall, or sensitivity, quantifies the proportion of actual positive samples correctly identified by the model, indicating its ability to minimize false negatives. Precision evaluates the proportion of predicted positive samples that are truly positive, representing the reliability of positive predictions and the ability to reduce false alarms. The F_1 -score, defined as the harmonic mean of precision and recall, provides a balanced measure of both sensitivity and specificity, particularly useful when class distributions are imbalanced. Additionally, the AUC-ROC (area under the receiver operating characteristic curve) was computed to assess discriminative capability of a model across varying decision thresholds. A higher AUC indicates a stronger separation between positive and negative classes.

A. Performance from scratch

Table III summarizes the experimental results of the five CNN architectures trained on SARS-CoV-2 Circos image datasets corresponding to different viral variants. Overall, all models achieved high classification accuracy, demonstrating that convolutional architectures can effectively capture the epistatic patterns embedded in the genomic interaction images.

Among the classical VGG networks, VGG13 slightly outperformed VGG16, achieving a weighted average F_1 -

score of 93.91% compared with 90.87% for VGG16. The deeper structure of VGG16 likely introduced additional parameters without providing proportional performance gains, leading to mild overfitting.

In contrast, lightweight models such as MobileNetV3 exhibited significantly improved generalization, with a weighted F_1 -score of 96.19% and an AUC of 0.999886, reflecting both high accuracy and computational efficiency. Similarly, DenseNet121 achieved strong and stable results, yielding a weighted F_1 -score of 97.46% and an AUC of 0.999265, confirming the benefit of dense connectivity in feature propagation and gradient reuse.

The best overall performance was achieved by EfficientNet_B0, which reached a weighted F_1 -score of 97.45% and an AUC of 0.999271. Its compound scaling strategy effectively balances network depth, width, and resolution, enabling superior feature extraction with fewer parameters. The consistency between F_1 -score and AUC across all architectures indicates robust classification of variant-specific genomic patterns.

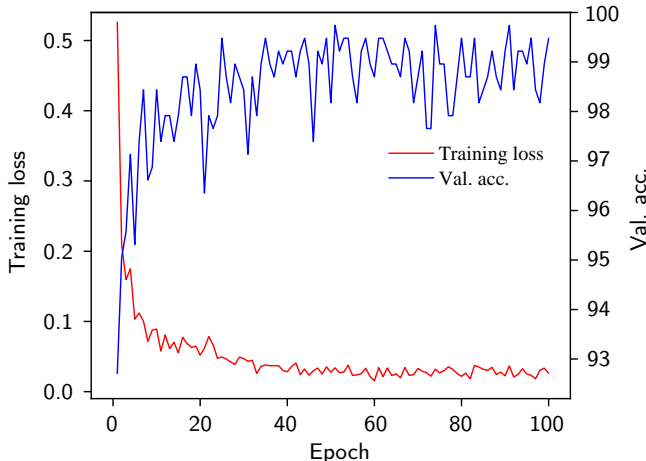


FIG. 4: Training loss and validation accuracy curves of the DenseNet121 model over 100 epochs. The training loss decreases steadily while the validation accuracy remains consistently high, indicating stable convergence and strong generalization without overfitting.

To illustrate the training and convergence behavior of the models, the training dynamics of DenseNet121 as a representative example were shown in Figure 4. The training loss (red curve) decreases rapidly during the initial 20 epochs and gradually stabilizes near zero, while the validation accuracy (blue curve) remains consistently above 98%, indicating efficient optimization and robust generalization without overfitting. Such behaviors are benefit from the dense connectivity of DenseNet, which enhances gradient flow and feature reuse across layers, resulting in faster convergence and reduced parameter redundancy. The stable learning pattern further confirms that the chosen training strategy and hyperparameter configuration in Table II were appropriate for the classification of SARS-CoV-2 epistatic interaction images.

These convergence characteristics are consistent across other CNN architectures and provide a solid foundation for the subsequent comparative performance analysis.

B. Performance from transfer learning

The classification results in Table III were obtained from models trained with randomly initialized weights. To enhance convergence speed and generalization performance, we subsequently fine-tuned the same architectures using pre-trained weights derived from the ImageNet dataset. In transfer learning, low- and mid-level visual features such as edges, textures, and shapes, which are learned from large-scale natural image corpora like ImageNet, are generally transferable across tasks. To balance the contribution of different feature levels, lower convolutional layers are typically frozen to retain general visual representations, while higher layers are fine-tuned to adapt to task-specific semantics. This hierarchical adjustment allows the model to leverage generic visual priors while maintaining flexibility for the new classification of the SARS-CoV-2 Circos image dataset here. Meanwhile, the learning rate was reduced by an order of magnitude relative to the initial training (e.g., from 3.125×10^{-3} to 3.125×10^{-4}) to prevent the degradation of pre-trained features. Data augmentation techniques such as random rotation, horizontal flipping, and scaling were again applied to improve model generalization.

The transfer learning strategy led to faster convergence and higher stability across all architectures, as the models required fewer epochs to reach optimal validation accuracy. In particular, EfficientNet_B0 and DenseNet121 exhibited notable gains in both F_1 -score and AUC, confirming that pre-trained representations significantly facilitate the learning of genomic epistatic interaction patterns.

1. Comparative Analysis between Random Initialization and Transfer Learning

The results in Table IV clearly shows the substantial performance improvement achieved through transfer learning. When initialized with pre-trained ImageNet weights, all five CNN architectures exhibited faster convergence, higher classification accuracy, and stronger generalization across variant categories. Specifically, the weighted average F_1 -scores of all models improved by approximately 2-3 percentage, while the AUC values increased consistently, all exceeding 0.9994. The gain was most pronounced for DenseNet121 and EfficientNet_B0, whose weighted F_1 -scores reached 99.27%, marking an improvement of nearly 1.8% over their randomly initialized counterparts. These two architectures benefited the most from fine-tuning, as the dense connectivity in DenseNet and compound scaling in EfficientNet facilitate efficient adaptation of pre-trained representations to the

TABLE III: Performance comparison of five CNN architectures on SARS-CoV-2 Circos image datasets corresponding to different viral variants.

Models	Class	Precision	Recall	F_1 -score	AUC
VGG-13	Alpha	95.05	93.2	94.12	0.995830
	Delta	94.23	95.15	94.69	
	Omicron	91.49	96.63	93.99	
	Else	94.79	91	92.86	
	WeightedAvg.	93.89	93.99	93.91	
VGG-16	Alpha	93.94	90.29	92.08	0.989148
	Delta	88.89	93.2	91	
	Omicron	88.3	93.26	90.71	
	Else	92.55	87	89.69	
	WeightedAvg.	90.92	90.94	90.87	
MobileNetV3	Alpha	95.28	98.06	96.65	0.998986
	Delta	98.99	95.15	97.03	
	Omicron	95.56	96.63	96.09	
	Else	95	95	95	
	WeightedAvg.	96.21	96.21	96.19	
DenseNet121	Alpha	95.33	99.03	97.14	0.999265
	Delta	100	97.09	98.52	
	Omicron	96.67	97.75	97.21	
	Else	97.96	96	96.97	
	WeightedAvg.	97.49	97.47	97.46	
EfficientNet_b0	Alpha	98.99	95.15	97.03	0.999271
	Delta	97.14	99.03	98.08	
	Omicron	98.84	95.51	97.14	
	Else	95.24	100	97.56	
	WeightedAvg.	97.55	97.42	97.45	

SARS-CoV-2 Circos images.

Furthermore, the improvement in VGG-13 and VGG-16 indicates that even classical CNNs gain notable advantages from transfer learning, particularly in recall and stability across smaller variant classes. The uniformly high precision and recall values (each above 97%) across all architectures suggest that pre-trained weights not only accelerate optimization but also effectively prevent overfitting to specific strain-level data distributions.

C. Dropout Ablation Study

To investigate whether additional regularization could further enhance robustness under transfer learning, we applied a Dropout layer to the classifier and re-evaluated all five CNN architectures. As shown in Table V, however, introducing Dropout consistently decreased overall performance across all models, with weighted average F_1 -scores dropping by approximately 1–1.5% compared with the non-Dropout transfer-learning results (Table IV).

This degradation is likely due to the fact that, under transfer learning, the convolutional backbone is initialized with highly stable and well-generalized feature representations learned from large-scale datasets. In this setting, the addition of stochastic deactivation disrupts the structured feature space inherited from the pre-trained

model, weakening the discriminative capacity of the high-level representations.

Moreover, the Circos images used in this study encode global epistatic interaction patterns, where the removal of randomly selected activations can obscure informative long-range dependencies, thus leading to inferior classification performance.

These findings indicate that transfer learning already provides sufficient regularization, and that additional Dropout is not only unnecessary but may even be detrimental for SARS-CoV-2 variant classification. Therefore, all final models in this work were trained without Dropout during fine-tuning.

D. Confusion Matrix and ROC curves

The confusion matrix of the EfficientNet_B0 classifier (Fig.5) exhibits a nearly ideal diagonal structure, reflecting highly consistent class-wise prediction fidelity across all four SARS-CoV-2 lineages. Misclassification events are extremely sparse and restricted to a minor degree of reciprocal confusion between Alpha and Delta, two variants known to share partially overlapping mutational profiles during specific transmission periods. In contrast, Omicron and the aggregated Else category are resolved with perfect or near-perfect accuracy, indicating that the

TABLE IV: Experimental results of five models using transfer learning with different virulent strain data samples

Models	Class	Precision	Recall	F1-score	AUC
VGG-13	Alpha	98.1	100	99.04	0.999554
	Delta	100	99.03	99.51	
	Omicron	98.88	98.88	98.88	
	Else	97.98	97	97.49	
	WeightedAvg.	98.74	98.73	98.73	
VGG-16	Alpha	96.19	98.06	97.12	0.999503
	Delta	99.01	97.09	98.04	
	Omicron	97.78	98.88	98.32	
	Else	96.97	96	96.48	
	WeightedAvg.	97.49	97.51	97.49	
MobileNetV3	Alpha	99.02	98.06	98.54	0.999436
	Delta	100	98.06	99.02	
	Omicron	96.67	97.75	97.21	
	Else	96.08	98	97.03	
	WeightedAvg.	97.94	97.97	97.95	
DenseNet121	Alpha	99.03	99.03	99.03	0.999950
	Delta	99.02	98.06	98.54	
	Omicron	100	100	100	
	Else	99.01	100	99.5	
	WeightedAvg.	99.26	99.27	99.27	
EfficientNet_B0	Alpha	99.03	99.03	99.03	0.999899
	Delta	100	98.06	99.02	
	Omicron	100	100	100	
	Else	98.04	100	99.01	
	WeightedAvg.	99.27	99.27	99.26	

model successfully captures the distinctive epistatic interaction signatures characterizing these lineages.

This pattern suggests that the convolutional features extracted from Circos-based epistasis representations contain sufficiently rich and lineage-specific structure to enable robust differentiation, even in cases where genomic backgrounds exhibit substantial evolutionary convergence. The high diagonal dominance therefore highlights not only the model’s predictive strength, but also the discriminability of epistatic architectures across major SARS-CoV-2 clades.

Moreover, the ROC curves in Figure 6 further substantiate the classifier’s exceptional discriminative capacity. All variant-specific ROC trajectories converge toward the top-left corner, and the near-perfect overlap between the micro- and macro-averaged curves indicates uniformly strong performance across both frequent and less abundant classes. AUC values approaching 1.0 demonstrate that the learned feature embeddings provide a highly stable decision boundary, insensitive to threshold variation and free from class-imbalance degradation.

These results imply that the Circos epistasis used as model inputs encode global interaction patterns that remain separable under a broad range of classification thresholds. Such robustness is particularly noteworthy in the context of rapidly evolving viral genomes, where shifts in allele frequencies and combinatorial interactions could otherwise obscure lineage boundaries. The

ROC analysis therefore reinforces the conclusion that the model captures biologically meaningful epistatic structures with high generalization capability.

To validate the interpretability of the EfficientNet_B0 model and understand the morphological features driving the classification of SARS-CoV-2 variants, we employed Gradient-weighted Class Activation Mapping (Grad-CAM). As shown in Figure 7, the model demonstrates distinct attention patterns corresponding to the unique genomic mutation linkages of each strain. For the Alpha variant, the “heat” focus is prominently concentrated in the central region of the Circos plot, suggesting a reliance on a specific convergence of mutation links. In contrast, the Delta variant exhibits a broader, horizontally distributed activation region slightly offset to the left, capturing a wider network of genomic interactions. Notably, the Omicron variant triggers a highly localized activation in the upper-left quadrant, distinguishing it from the central focus observed in the “Else” category. These visual evidences confirm that the classifier does not rely on background artifacts or peripheral noise (such as the outer scale ring); instead, it effectively extracts discriminative topological features—specifically the intersection and density of internal chords representing mutation relationships—to achieve robust classification.

TABLE V: Experimental results for the five models after using the Dropout layer under the use of transfer learning

Models	Class	Precision	Recall	F1-score	AUC
VGG-13	Alpha	98.06	98.06	98.06	0.999388
	Delta	98.1	100	99.04	
	Omicron	97.73	96.63	97.18	
	Else	96.97	96	96.48	
	WeightedAvg.	97.71	97.67	97.69	
VGG-16	Alpha	98.06	98.06	98.06	0.999740
	Delta	99.04	100	99.52	
	Omicron	97.78	98.88	98.32	
	Else	97.96	96	96.97	
	WeightedAvg.	98.21	98.23	98.22	
MobileNetV3	Alpha	100	95.15	97.51	0.999225
	Delta	98.04	97.09	97.56	
	Omicron	94.57	97.75	96.13	
	Else	95.15	98	96.55	
	WeightedAvg.	96.94	97	96.94	
DenseNet121	Alpha	99.01	97.09	98.04	0.999435
	Delta	100	100	100	
	Omicron	94.68	100	97.27	
	Else	96.91	94	95.43	
	WeightedAvg.	97.65	97.77	97.68	
EfficientNet_B0	Alpha	99.04	100	99.52	0.999777
	Delta	100	97.09	98.52	
	Omicron	97.8	100	98.89	
	Else	98	98	98	
	WeightedAvg.	98.71	98.77	98.73	

IV. DISCUSSION

The evolution of SARS-CoV-2 has been characterized by the recurrent emergence of highly divergent lineages with distinct phenotypic profiles, including altered transmissibility, immune escape potential, and host-range adaptation. Understanding the genomic determinants of these phenotypic shifts requires analytical approaches that can detect not only individual mutations but also the coordinated mutational processes that shape viral adaptation. Our study demonstrates that epistatic interaction patterns inferred from large-scale SARS-CoV-2 sequences contain rich biological information about how variants diversify and adapt, and that these patterns are sufficiently distinctive to enable near-perfect lineage classification using deep learning.

The strong lineage-specific separability observed in our epistatic maps reflects the fact that SARS-CoV-2 evolution is highly modular. Major variants such as Alpha, Delta, and Omicron exhibit characteristic constellations of mutations that arise in the context of strong selective pressures—particularly immune evasion and enhanced receptor binding. These constellations are not random collections of substitutions; rather, they represent co-evolving mutational modules shaped by both functional requirements and structural constraints of the viral proteome. For example, Omicron’s extensive set of Spike mutations includes both destabilizing and compen-

satory changes, forming tightly integrated epistatic networks that allow the lineage to escape neutralizing antibodies while maintaining receptor affinity. The DCA-inferred couplings recovered in our study recapitulate these known biological patterns, suggesting that the statistical signatures captured by our method correspond to genuine co-adaptive interactions in the viral genome.

The rare misclassification between Alpha and Delta further reinforces the biological realism of our findings. Although these lineages are phylogenetically distant, both experienced phases of rapid global spread and independently acquired recurrent mutations in genomic regions under strong selective pressure, such as Spike NTD and RBD residues implicated in immune evasion. These episodes of convergent evolution create partial overlap in their epistatic profiles, explaining the slight ambiguity observed in the model’s predictions. Such patterns underscore the importance of analyzing SARS-CoV-2 evolution not solely through phylogenetic divergence but also through the lens of shared adaptive pathways and repeated mutational solutions.

The results highlight that the epistatic landscape of SARS-CoV-2 is highly structured, with major lineages occupying distinct regions of the underlying fitness landscape. This structure arises from evolutionary constraints imposed by protein stability, replication machinery fidelity, host receptor usage, and immune selection. The fact that these constraints manifest so clearly in

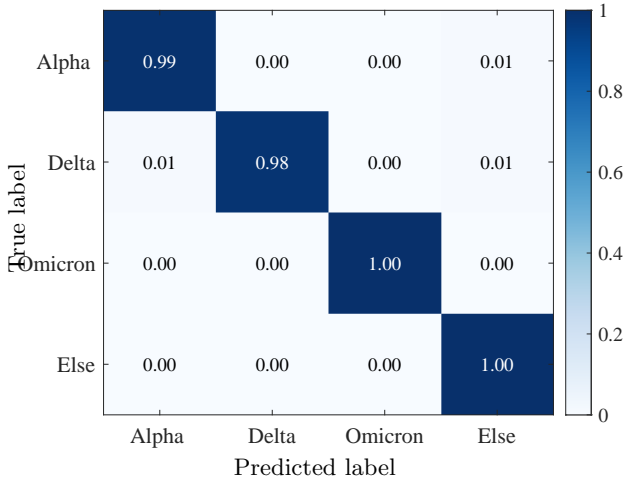


FIG. 5: Confusion matrix of the DenseNet121 model with transfer learning setting for predicting SARS-CoV-2 variant classes from DCA-derived epistatic interaction images. Values represent normalized prediction frequencies for the four variant categories (Alpha, Delta, Omicron, and Else). The strong diagonal dominance indicates near-perfect classification performance, with only minor reciprocal confusion between Alpha and Delta and perfect separation for Omicron and the composite Else class. This matrix highlights the discriminability of lineage-specific epistatic structures captured by the model.

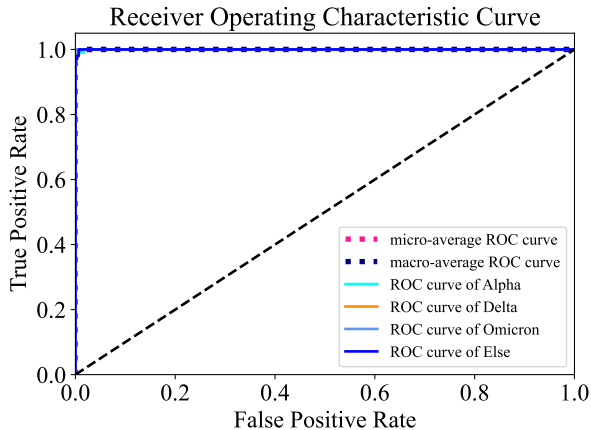


FIG. 6: Receiver operating characteristic (ROC) curves for the DenseNet121 classifier evaluated on the SARS-CoV-2 epistasis image dataset. Curves are shown for each variant class as well as for the micro- and macro-averaged performance across all classes. All ROC trajectories lie near the top-left corner, with area-under-the-curve (AUC) values approaching 1.0, demonstrating excellent threshold-independent discrimination and robust separability of variant-specific epistatic patterns.

DCA-inferred couplings suggests that pairwise epistasis

captures a substantial portion of the selective architecture governing SARS-CoV-2 evolution. The ability of CNNs to learn higher-order patterns from these couplings implies that even more complex interactions—beyond pairwise correlations—may be encoded in the Circos-derived epistatic geometries.

The findings here suggest that lineage-specific epistatic signatures may serve as predictive markers of evolutionary potential, offering insight into which mutational combinations are selectively favored or disfavored under different epidemiological conditions. As new variants continue to emerge, the integrative framework presented here could support early detection of unusual epistatic configurations that signal shifts in antigenicity, host adaptation, or transmission patterns. More broadly, this work demonstrates that combining population-genetic theory, coevolutionary inference, and deep learning provides a powerful approach to dissecting the mechanistic basis of viral evolution.

V. CONCLUSION

We developed an integrated framework that combines population-genetic theory, statistical epistasis inference, and deep learning to classify SARS-CoV-2 genomic variants through their epistatic interaction signatures in this study. By applying DCA approach under the QLE approximation, we derived lineage-specific coupling patterns that capture coordinated mutational dependencies shaped by the virus’s evolutionary history. Circos-based visualizations of these epistatic networks provided a compact and interpretable representation of the global interaction structure, from which CNNs were able to extract robust discriminative features.

Across multiple architectures, transfer learning markedly enhanced classification accuracy, with DenseNet121 and EfficientNet_B0 achieving near-perfect performance. Confusion matrix and ROC analyses further confirmed the strong separability of epistatic landscapes across SARS-CoV-2 variants, indicating that the major lineages occupy distinct regions of the fitness landscape shaped by co-evolving mutational modules. These results validate not only the predictive capability of the proposed approach but also the biological relevance of DCA-inferred epistatic couplings as a meaningful descriptor of viral evolutionary constraints.

The methodological framework introduced here offers several promising directions for future genomic surveillance and evolutionary inference. First, the ability of deep networks to detect lineage-specific epistatic signatures from DCA-derived coupling maps suggests that this approach may be extended to emerging variants in real time, even before large-scale phylogenetic characterization is available. By continuously updating MSAs and recalculating coupling structures, the system could provide an early-warning signal when novel epistatic patterns deviate from established lineages, potentially indi-

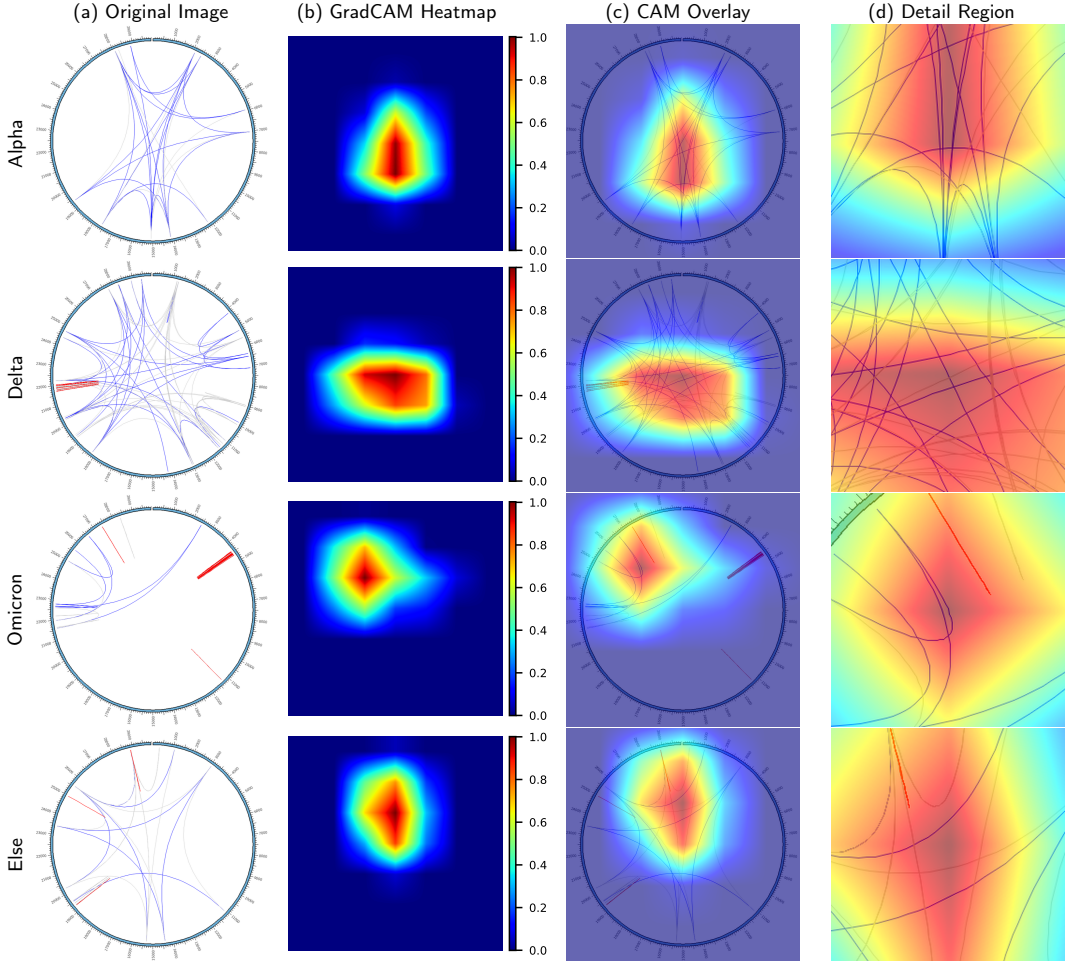


FIG. 7: Visualization of EfficientNet_B0 decision-making regions for SARS-CoV-2 strain classification using GradCAM. The figure illustrates the model’s attention mechanisms across four distinct classes: Alpha, Delta, Omicron, and Else. (a) The original input images representing genomic data as Circos plots. (b) The generated GradCAM heatmaps, where red regions indicate high activation values and blue regions represent low activation. (c) The overlay of the heatmap onto the original image, highlighting the specific structural features contributing to the classification. (d) A magnified view of the most salient regions. The visualization reveals that the model learns to identify strain-specific topological patterns and linkage densities within the genomic interaction networks to distinguish between variants.

cating shifts in transmissibility, immune escape potential, or host adaptation.

Second, because DCA captures pairwise epistasis but CNNs can implicitly learn higher-order dependencies, this hybrid framework is well positioned to reveal complex interaction modules that underlie major adaptive transitions. Such modules may correspond to compensatory mutational clusters or structural integration motifs that define evolutionary accessible trajectories. Identifying these modules could enhance our understanding of the constraints shaping SARS-CoV-2 evolution and support predictive modeling of future lineage emergence.

Finally, the generality of the approach makes it directly applicable to other rapidly evolving pathogens—including influenza, HIV, and ar-

boviruses—where coordinated evolutionary processes play a central role in antigenic drift and escape. By integrating statistical physics-based inference with modern computer vision, the framework bridges mechanistic modeling and data-driven prediction, providing a powerful tool for real-time genomic monitoring, evolutionary forecasting, and functional interpretation of mutational landscapes.

ACKNOWLEDGEMENTS

The work of BJ, HLZ was sponsored by the National Natural Science Foundation of China (11705097), the China Scholarship Council (202508320441), and the Nat-

ural Science Foundation of Nanjing University of Posts and Telecommunications (Grant No. 221101, 222134). EA acknowledges support from the Swedish Research

Council through grant 2020-04980.

DECLARATIONS

There is no Conflict of interest.

[1] World health organization. <https://covid19.who.int/>. Accessed June 2025.

[2] William T Harvey, Alessandro M Carabelli, Ben Jackson, Ravindra K Gupta, Emma C Thomson, Ewan M Harrison, Catherine Ludden, Richard Reeve, Andrew Rambaut, COVID-19 Genomics UK (COG-UK) Consortium, et al. Sars-cov-2 variants, spike mutations and immune escape. *Nature reviews microbiology*, 19(7):409–424, 2021.

[3] Freunde von GISAID e.V. Gisaid. <https://www.gisaid.org/>. Accessed 2022.

[4] Alief Moulana, Thomas Dupic, Angela M Phillips, Jeffrey Chang, Serafina Nieves, Anne A Roffler, Allison J Greaney, Tyler N Starr, Jesse D Bloom, and Michael M Desai. Compensatory epistasis maintains ace2 affinity in sars-cov-2 omicron ba. 1. *Nature communications*, 13(1):7011, 2022.

[5] Leander Witte, Viren A Baharani, Fabian Schmidt, Zijun Wang, Alice Cho, Raphael Raspe, Camila Guzman-Cardozo, Frauke Muecksch, Marie Canis, Debby J Park, et al. Epistasis lowers the genetic barrier to sars-cov-2 neutralizing antibody escape. *Nature communications*, 14(1):302, 2023.

[6] Magnus Ekeberg, Cecilia Lökvist, Yueheng Lan, Martin Weigt, and Erik Aurell. Improved contact prediction in proteins: Using pseudolikelihoods to infer potts models. *Phys. Rev. E*, 87:012707, January 2013.

[7] Magnus Ekeberg, Tuomo Hartonen, and Erik Aurell. Fast pseudolikelihood maximization for direct-coupling analysis of protein structure from many homologous amino-acid sequences. *J. Comput. Phys.*, 276:341–356, 2014.

[8] Alexander Schug, Martin Weigt, José N Onuchic, Terence Hwa, and Hendrik Szurmant. High-resolution protein complexes from integrating genomic information with molecular simulation. *Proceedings of the National Academy of Sciences*, 106(52):22124–22129, 2009.

[9] Hong-Li Zeng, Vito D’Alio, Edwin Rodríguez Horta, Kaisa Thorell, and Erik Aurell. Global analysis of more than 50,000 SARS-CoV-2 genomes reveals epistasis between eight viral genes. *Proceedings of the National Academy of Sciences*, 117(49):31519–31526, 2020.

[10] Hong-Li Zeng, Yue Liu, Vito D’Alio, and Erik Aurell. Temporal epistasis inference from more than 3,500,000 SARS-CoV-2 genomic sequences. *Phys. Rev. E*, 106:044409, Oct 2022.

[11] Hong-Li Zeng, Cheng-Long Yang, Bo Jing, John Barton, and Erik Aurell. Two fitness inference schemes compared using allele frequencies from 1068 391 sequences sampled in the uk during the covid-19 pandemic. *Physical Biology*, 22(1):016003, nov 2025.

[12] Martin Krzywinski, Jacqueline Schein, Inanc Birol, Joseph Connors, Randy Gascoyne, Doug Horsman, Steven J Jones, and Marco A Marra. Circos: an information aesthetic for comparative genomics. *Genome research*, 19(9):1639–1645, 2009.

[13] Yann LeCun, Yoshua Bengio, and Geoffrey Hinton. Deep learning. *nature*, 521(7553):436–444, 2015.

[14] Alex Krizhevsky, Ilya Sutskever, and Geoffrey E Hinton. Imagenet classification with deep convolutional neural networks. *Advances in neural information processing systems*, 25, 2012.

[15] Andrew W Senior, Richard Evans, John Jumper, James Kirkpatrick, Laurent Sifre, Tim Green, Chongli Qin, Augustin Žídek, Alexander WR Nelson, Alex Bridgland, et al. Improved protein structure prediction using potentials from deep learning. *Nature*, 577(7792):706–710, 2020.

[16] Jacob Schreiber, Timothy Durham, Jeffrey Bilmes, and William Stafford Noble. Avocado: a multi-scale deep tensor factorization method learns a latent representation of the human epigenome. *Genome biology*, 21(1):81, 2020.

[17] Jian Zhou and Olga G Troyanskaya. Predicting effects of noncoding variants with deep learning-based sequence model. *Nature methods*, 12(10):931–934, 2015.

[18] Alejandro Lopez-Rincon, Alberto Tonda, Lucero Mendoza-Maldonado, Daphne G. J. C. Mulders, Richard Molenkamp, Carmina A. Perez-Romero, Eric Claassen, Johan Garssen, and Aletta D. Kraneveld. Classification and specific primer design for accurate detection of sars-cov-2 using deep learning. *Scientific Reports*, 11(1):947, Jan 2021.

[19] Kishan Kalia, Gayatri Saberwal, and Gaurav Sharma. The lag in SARS-CoV-2 genome submissions to gisaid. *Nature Biotechnology*, 39(9):1058–1060, 2021.

[20] Kazutaka Katoh, John Rozewicki, and Kazunori D Yamada. Mafft online service: multiple sequence alignment, interactive sequence choice and visualization. *Briefings in bioinformatics*, 20(4):1160–1166, 2019.

[21] Shigehiro Kuraku, Christian M Zmasek, Osamu Nishimura, and Kazutaka Katoh. aleaves facilitates on-demand exploration of metazoan gene family trees on mafft sequence alignment server with enhanced interactivity. *Nucleic acids research*, 41(W1):W22–W28, 2013.

[22] Fan Wu, Su Zhao, Bin Yu, Yan-Mei Chen, Wen Wang, Zhi-Gang Song, Yi Hu, Zhao-Wu Tao, Jun-Hua Tian, Yuan-Yuan Pei, et al. A new coronavirus associated with human respiratory disease in china. *Nature*, 579(7798):265–269, 2020.

[23] Hong-Li Zeng, Vito D’Alio, Edwin Rodríguez Horta, Kaisa Thorell, and Erik Aurell. Global analysis of more than 50,000 SARS-CoV-2 genomes reveals epistasis between eight viral genes. *Proceedings of the National Academy of Sciences*, 117(49):31519–31526, 2020.

[24] Martin Weigt, Robert A. White, Hendrik Szurmant, James A. Hoch, and Terence Hwa. Identification of direct residue contacts in protein–protein interaction by

message passing. *Proceedings of the National Academy of Sciences*, 106(1):67–72, 2009.

[25] Faruck Morcos, Andrea Pagnani, Bryan Lunt, Arianna Bertolino, Debora S. Marks, Chris Sander, Riccardo Zecchina, José N. Onuchic, Terence Hwa, and Martin Weigt. Direct-coupling analysis of residue coevolution captures native contacts across many protein families. *Proceedings of the National Academy of Sciences*, 108(49):E1293–E1301, 2011.

[26] Thomas A Hopf, Charlotta P I Schärfe, João P G L M Rodrigues, Anna G Green, Oliver Kohlbacher, Chris Sander, Alexandre M J J Bonvin, and Debora S Marks. Sequence co-evolution gives 3d contacts and structures of protein complexes. *eLife*, 3:e03430, Sep 2014.

[27] Riccardo Zecchina H. Chau Nguyen and Johannes Berg. Inverse statistical problems: from the inverse ising problem to data science. *Advances in Physics*, 66(3):197–261, 2017.

[28] Simona Cocco, Christoph Feinauer, Matteo Figliuzzi, Rími Monasson, and Martin Weigt. Inverse statistical physics of protein sequences: a key issues review. *Reports on progress in physics*, 81:032601, Mar 2018.

[29] Erik Aurell. The Maximum Entropy Fallacy Redux? *PLoS computational biology*, 12:e1004777, May 2016.

[30] Erik van Nimwegen. Inferring Contacting Residues Within and Between Proteins: What Do the Probabilities Mean? *PLoS computational biology*, 12:e1004726, May 2016.

[31] Motoo Kimura. Attainment of quasi linkage equilibrium when gene frequencies are changing by natural selection. *Genetics*, 52(5):875–890, 1965.

[32] Richard A. Neher and Boris I. Shraiman. Competition between recombination and epistasis can cause a transition from allele to genotype selection. *Proc. Natl. Acad. Sci.*, 106(16):6866–6871, 2009.

[33] Richard A. Neher and Boris I. Shraiman. Statistical genetics and evolution of quantitative traits. *Rev. Mod. Phys.*, 83:1283–1300, Nov 2011.

[34] Chen-Yi Gao, Fabio Cecconi, Angelo Vulpiani, Hai-Jun Zhou, and Erik Aurell. Dca for genome-wide epistasis analysis: the statistical genetics perspective. *Physical biology*, 16(2):026002, 2019.

[35] Hong-Li Zeng and Erik Aurell. Inferring genetic fitness from genomic data. *Phys. Rev. E*, 101:052409, May 2020.

[36] Vito Dichtio, Hong-Li Zeng, and Erik Aurell. Statistical genetics in and out of quasi-linkage equilibrium. *Reports on Progress in Physics*, 86(5):052601, apr 2023.

[37] Richard A Neher, Marija Vucelja, Mark Mezard, and Boris I Shraiman. Emergence of clones in sexual populations. *Journal of Statistical Mechanics: Theory and Experiment*, 2013(01):P01008, jan 2013.

[38] Julian Besag. Statistical analysis of non-lattice data. *Journal of the Royal Statistical Society: Series D (The Statistician)*, 24(3):179–195, 1975.

[39] Pradeep Ravikumar, Martin J Wainwright, and John D Lafferty. High-dimensional Ising model selection using \mathcal{L}_1 regularized logistic regression. *The Annals of Statistics*, 38(3):1287–1319, 2010.

[40] Erik Aurell and Magnus Ekeberg. Inverse ising inference using all the data. *Physical review letters*, 108(9):090201, 2012.

[41] Magnus Ekeberg, Cecilia Lökvist, Yueheng Lan, Martin Weigt, and Erik Aurell. Improved contact prediction in proteins: using pseudolikelihoods to infer potts models. *Physical Review E*, 87(1):012707, 2013.

[42] Magnus Ekeberg, Tuomo Hartonen, and Erik Aurell. Fast pseudolikelihood maximization for direct-coupling analysis of protein structure from many homologous amino-acid sequences. *Journal of Computational Physics*, 276:341–356, 2014.

[43] JingBo. Data from "xiaohuolongx/circos-data-set." github. <https://github.com/xiaohuolongx/circos-data-set.git>, 2023.

[44] Zewen Li, Fan Liu, Wenjie Yang, Shouheng Peng, and Jun Zhou. A survey of convolutional neural networks: analysis, applications, and prospects. *IEEE transactions on neural networks and learning systems*, 2021.

[45] Karen Simonyan and Andrew Zisserman. Very deep convolutional networks for large-scale image recognition. *arXiv preprint arXiv:1409.1556*, 2014.

[46] Andrew G Howard, Menglong Zhu, Bo Chen, Dmitry Kalenichenko, Weijun Wang, Tobias Weyand, Marco Andreetto, and Hartwig Adam. Mobilenets: Efficient convolutional neural networks for mobile vision applications. *arXiv preprint arXiv:1704.04861*, 2017.

[47] Andrew Howard, Mark Sandler, Grace Chu, Liang-Chieh Chen, Bo Chen, Mingxing Tan, Weijun Wang, Yukun Zhu, Ruoming Pang, Vijay Vasudevan, et al. Searching for mobilenetv3. In *Proceedings of the IEEE/CVF international conference on computer vision*, pages 1314–1324, 2019.

[48] Gao Huang, Zhuang Liu, Laurens Van Der Maaten, and Kilian Q Weinberger. Densely connected convolutional networks. In *Proceedings of the IEEE conference on computer vision and pattern recognition*, pages 4700–4708, 2017.

[49] Mingxing Tan and Quoc Le. Efficientnet: Rethinking model scaling for convolutional neural networks. In *International conference on machine learning*, pages 6105–6114. PMLR, 2019.